Microchannel plate response to solar energetic particles and consequences for solar-wind measurements on ESA's Vigil mission

P.-Y. Parent,[1,2]★ D. Verscharen ![ORCID],[2]★ G. Nicolaou[2] and C. J. Owen[2]

[1]*Département de Physique de l'École Polytechnique, Institut Polytechnique de Paris, Palaiseau 91120, France*
[2]*Mullard Space Science Laboratory, University College London, Dorking RH5 6NT, UK*

ABSTRACT

Space weather forecasting aims at predicting the impacts of the Sun, interplanetary space, and the planetary environment on biological and technological systems. To monitor space weather, the European Space Agency is developing the *Vigil* mission. *Vigil* will carry the Plasma Analyser (PLA) instrument. We investigate the expected impact of Solar Energetic Particles (SEPs) on PLA. We analyse previous measurements from Solar Orbiter's Solar Wind Analyser (SWA) Electron Analyser System (EAS) that, like PLA, uses a microchannel plate (MCP) as its detector. Using a fitting algorithm, we extract the number of erroneous counts created by the interaction between SEPs and the MCP. Using SEP flux measurements from Solar Orbiter's Energetic Particle Detector (EPD) and multilinear regression, we establish a linear relationship between the number of erroneous counts and SEP fluxes. We define an SEP index, characterizing the impact of SEP events on EAS measurements. We then simulate PLA measurements during SEP events characterized by their SEP index. We show that moderate SEP events cause significant discrepancies in PLA plasma moment estimations under common solar-wind conditions. Based on our results, we propose a correction method for erroneous counts created by SEPs in instruments such as EAS and PLA.

Key words: Plasma – Instrumentation – Energetic particles – Noise – Numerical methods.

1 INTRODUCTION

1.1 Space plasma measurements and context

The study of space plasmas is a key element of space science. Plasma is the most common state of baryonic matter in the universe. It is composed of free electrons and ions exhibiting collective behaviour which, under certain assumptions, allows us to use classical fluid variables such as density, bulk speed, and temperature to characterize the flow macroscopically. The solar wind is a flow of plasma emanating from the Sun, interacting with all the planets and bodies in the solar system (Formisano et al. 1973; Smith et al. 1974). The solar wind is a key source of space weather and constantly interacts with spacecraft (Baker 1998). In addition, solar flares and coronal mass ejections accelerate solar energetic particles (SEPs) that contribute to the impact of space weather (Reames 2015; Temmer 2021). Given the consequences that extreme space-weather events have for activities both in space and on the ground (Hands et al. 2018; Battersby 2019; Marov & Kuznetsov 2021), it is crucial to monitor solar activity and space weather. This motivated the European Space Agency to adopt the Vigil mission. Observing the Sun and *in-situ* conditions, the *Vigil* spacecraft will be located at the fifth Sun–Earth Lagrange point (L5). From this stable orbital position, *Vigil* will be able to observe structures on the solar surface up to five days before they become visible from Earth or L1, enabling early warning of space weather and relevant solar activity. This side view will also allow us to trace coronal mass ejections and evaluate the likeliness of their impact on Earth. The *Vigil* spacecraft will host five instruments: the Photospheric Magnetic field Imager (PMI; Staub et al. 2020), the Heliospheric Imager (HI), the Compact Coronagraph (CCOR), the Joint EUV coronal Diagnostic Investigation (JEDI), the Magnetometer (MAG; Eastwood et al. 2024), and the Plasma Analyser (PLA).

The latter two instruments (MAG and PLA) represent the *in-situ* payload of the spacecraft. These instruments will quantitatively characterize the plasma and magnetic-field environment at L5, enabling, for instance, the forecasting of fast solar-wind streams and co-rotating interaction regions 4 to 5 d before they point towards Earth. In this context, PLA will provide the properties of protons in the solar-wind plasma and, in particular, allow us to deduce their density, bulk velocity, and temperature of the plasma (Nicolaou et al. 2020; Zhang, Verscharen & Nicolaou 2024).In addition, these *in-situ* measurement points will serve as fixed points for global space-weather models. The *Vigil* payload does not include an energetic particle detector, which limits our ability to investigate the impact of energetic particles on the performance of PLA in flight. In this study, we thus develop alternative approaches to account for the impact of energetic particles on PLA measurements.

1.2 Sensitivity of plasma analysers

The operating principle of plasma analysers such as PLA is to determine the velocity distribution functions (VDFs) of all the species in the plasma and then derive the moments of the VDFs: density, bulk speed, temperature, etc. An electrostatic plasma

---

★ E-mail: pierre-yves.parent.2020@polytechnique.org (P-YP);
d.verscharen@ucl.ac.uk (DV)
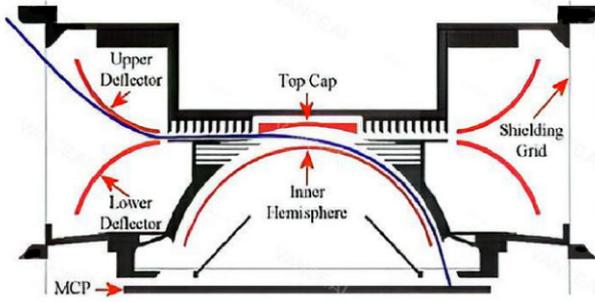
Figure 1. Cross-section of the optical model of the Improved Plasma Analyser (IPA). The line coming from the top left corner represents the path of an incoming particle. It is first deflected by the deflectors, which select the elevation of the accepted particles, and by the inner hemispheres, which select the energy per charge of the accepted particles. Finally, the particle reaches the MCP and is detected.

analyser accumulates counts of particles in energy, azimuth, and elevation. It thus builds up the full 3D VDF of a species in the plasma (Carlson et al. 1982).

Vigil's PLA is such an electrostatic analyser (see Fig. 1). It uses aperture deflectors, designed to resolve 3D VDFs of the solar wind protons. By stepping through voltages that are applied to deflectors and the inner hemispheres, only particles within a certain elevation range can enter the instrument. Electrostatic deflection between the inner hemispheres selects, based on the applied voltages, ions within a given range of energy per charge. Selected particles reach the microchannel plate (MCP), an electron multiplier (Ladislas Wiza 1979). In the MCP, the incoming particles trigger an electron cascade, creating a macroscopic current which is then detected by one of nine anodes that resolve the azimuth direction of the particle. The PLA instrument inherits its technology from the Electron Analyser System (EAS) of Solar Orbiter (Müller et al. 2020; Owen et al. 2020), although EAS is designed to detect electrons. Both instruments are based on the Improved Plasma Analyser (IPA) design concept, which was developed at UCL's Mullard Space Science Laboratory.

Both PLA and EAS face hostile measurement conditions. For instance, galactic cosmic rays, ultraviolet and x-ray radiation, and SEPs can all deteriorate the measurements of the thermal plasma particles by creating secondary electrons on the instrument case or by interacting with the MCP of the instrument internally (Mitchell et al. 2016).

1.3 Solar energetic particles and MCP interaction

The MCP is a critical component of this type of instrument. The electrostatic particle optics (deflectors and hemispheres) ensure that only thermal particles reach the MCP and create an electron cascade. However, energetic particles, depending on their composition and energy, can penetrate the aluminium structure of the instrument case and directly impact the MCP – independently of the settings of the electrostatic particle optics – triggering an electron cascade and creating an erroneous detection signal in the anodes below the MCP. If interpreted as a legitimate particle signal, this erroneous detection modifies the measured VDF and leads to errors in the moment calculation (i.e. the determination of density, bulk velocity, and temperature of the thermal plasma). The impact of these erroneous detections due to SEPs is of particular relevance in the case of Vigil/PLA, since this instrument is supposed to be operational even during extreme space-weather events as part of the payload of an

operational space-weather mission. Based on mechanical and mass-budget considerations, the minimum shielding requirement of PLA is 2 mm of aluminium, which is equivalent to Solar Orbiter EAS's requirement (Owen et al. 2020).

1.4 From EAS measurements to PLA predictions

The goal of our study is to quantify the erroneous counts that are caused by penetrating SEPs in in-flight EAS data. We investigate the relation between the erroneous counts and the physical properties of the incoming flux of SEPs by establishing a quantitative relation based on multilinear regression. We then use this relation to predict the impact of incoming SEPs on the expected future measurements of PLA.

2 METHODS

2.1 Instruments

Based on the shared technology between PLA and EAS, we make extensive use of data from EAS and other instruments on Solar Orbiter to predict Vigil/PLA's response to SEP events. EAS is a top-hat type electrostatic analyser, composed of two heads, which allows us to measure the VDF of electrons in the thermal range (1–5000 eV). In 4 s, each of the two heads of EAS scans electrons with elevation between $-45°$ and $+45°$, over all azimuth angles (0–360°) and energies. The number of electron counts at each bin in speed U, elevation angle Θ, and azimuth Φ using the midpoint rule and ignoring dead time is given by (Nicolaou et al. 2020)

$$C_{\text{theo}}(U, \Theta, \Phi, t) = G(U, \Theta, \Phi) U^4 \Delta t \, f(U, \Theta, \Phi, t), \quad (1)$$

where f is the electron VDF, $G(U, \Theta, \Phi) = A_0 (\Delta U/U) \Delta\Theta\Delta\Phi$ is the effective geometric factor of the instrument, A_0 is the effective aperture of the instrument for $\Theta = 0°$, Δt is the acquisition time for each step, and ΔU, $\Delta\Theta$, and $\Delta\Phi$ are the acceptance widths in speed, elevation angle, and azimuth angle (Nicolaou et al. 2020). We assume that the measured VDF is approximately isotropic in the spacecraft reference frame, given the high thermal speed of electrons compared to the solar wind bulk speed (Boldyrev, Forest & Egedal 2020).

We also use data from the energetic particle detector (EPD; Rodríguez-Pacheco et al. 2020), in particular from the high energy telescope (HET), which measures fluxes of electrons with energy per charge between 0.4 and 10 MeV q^{-1} and of various ion species within energy per charge between 7 and 100 MeV q^{-1}. We also use EPD's suprathermal ion spectrograph (SIS), which measures fluxes of different ions between 0.1 and 8 MeV q^{-1}, and EPD's electron proton telescope (EPT), which measures fluxes of electrons between 30 and 400 keV.

For each of the sensors and for each SEP species, we introduce the aggregated flux

$$F_{\text{tot}} = \sum_{i=1}^{N} F(E_i), \quad (2)$$

where $F(E_i)$ is the flux of the considered SEP species measured by the considered instrument in the ith energy bin, and N is the number of energy bins.

2.2 Extraction of the background noise in EAS data

The EAS MCP has a dead time of $t_d = 10^{-7}$ s. If the instrument registers C_{mes} counts, the dead time must be corrected for in order

to relate the counts to the VDF via equation (1). We account for the dead time by estimating the number of detected counts C from the electron distribution if there were no dead time as (Zhang et al. 2024)

$$C = \frac{C_{\text{mes}}}{1 - \frac{t_{\text{d}}}{\Delta t} C_{\text{mes}}}, \tag{3}$$

where C_{mes} is the number of counts registered by the instrument. This accounting for the dead time has little impact on electron measurements with EAS except for dense and fast plasma but Nicolaou et al. (2020) show that its impact is more important for PLA due to the cold-beam nature of the solar-wind protons.

We set the number of registered counts $C(U, \Theta, \Phi, t)$ as the sum of detected electron counts C_{e^-} and background counts C_{BCK}:

$$C(U, \Theta, \Phi, t) = C_{\text{e}^-}(U, \Theta, \Phi, t) + C_{\text{BCK}}(t), \tag{4}$$

where $C_{\text{e}^-}(U, \Theta, \Phi, t)$ can be approximated by C_{theo} using the midpoint rule. The quantity $C_{\text{BCK}}(t)$ describes the number of counts triggered by SEPs during a sampling time window Δt. It follows a Poisson law of parameter $c(t)$, where $c(t)$ is the mean of the random variable $C_{\text{BCK}}(t)$. We assume that, for a given scanning time window, the number of erroneous counts depends only on the scanning duration (Plan 2014). We retain only the time dependence to highlight that the background counts, being caused by SEPs penetrating through the instrument shielding, do not depend on the settings of the instrument in terms of U, Θ, and Φ.

According to the central limit theorem, assuming that the discrete set $(c(t))_t$ varies slowly, there is a τ so that

$$c(t) \approx \overline{C_{\text{BCK,av}}(U, t)} = \frac{1}{n_t} \sum_{|t-s|<\tau} C_{\text{BCK,av}}(U, s), \tag{5}$$

where n_t is the number of steps time. The bar represents the empirical mean, and

$$C_{\text{BCK,av}}(U, t) = \frac{1}{n_\Theta n_\Phi} \sum_{\Theta, \Phi} C_{\text{BCK}}(U, \Theta, \Phi, t) \tag{6}$$

is the elevation-azimuth average of C_{BCK}, where n_Θ and n_Φ are the number of bins in azimuth and elevation, respectively.

By averaging the measured counts over angles and a given time period, we separate $c(t)$ from the ambient counts:

$$\overline{C_{\text{av}}(U, t)} = \overline{C_{\text{e}^-,\text{av}}(U, t)} + c(t), \tag{7}$$

where

To extract $c(t)$, we assume that the ambient electrons follow an isotropic κ-distribution with a negligible bulk speed, so that the distribution is independent of Θ and Φ (Pierrard & Lazar 2010; Livadiotis 2018). We separate the time interval into fixed-duration windows, for which we compute only one value of $c(t)$ through the fitting of the logarithm of $C_{\text{BCK,av}}$ to the logarithm of the counts C_κ given by a κ-distribution added to c:

$$C_\kappa = \log\left[n \frac{\Gamma(\kappa + 1)}{\Gamma(\kappa - 0.5)} \left(\frac{m}{2\pi k_{\text{B}}(\kappa - 1.5)T} \right)^{3/2} \right.$$
$$\left. \times \left(1 + \frac{mU^2}{2k_{\text{B}}(\kappa - 3/2)T} \right)^{-\kappa - 1} GU^4 \, \Delta t + c \right], \tag{8}$$

where k_{B} is the Boltzmann constant, m is the mass of an electron, and $\Gamma(x)$ is the Γ-function.

We solve the non-linear least-squares problem through the Trust Region Reflective algorithm (Watson 1978).

Table 1. Specifications used for the fitting of the averaged counts versus speed. The density n, the κ-index κ, the temperature T, and the parameter c are the fit parameters.

Parameter	Value
Averaging time window	12 min
Lower boundary of speed	265 km s^{-1}
Boundaries	
κ	[1.51, 20]
n	[10^6, 10^8] m^{-3}
T	[10^3, 5×10^6] K
c	[10^{-3}, 7]
Initial guess	
κ	4
n	3×10^6 m^{-3}
T	10^4 K
c	1

We average the measured counts over a time window of 12 min. While shorter averaging times would allow for the capturing of dynamic events, longer averaging times would increase the number of detected counts and thus the statistical reliability of our results. A careful trade-off of these aspects shows that a 12-min long averaging time window provides us with a reasonable compromise. In our fit routine, we only include counts with speed above a pre-defined lower boundary to remove undesired contributions from photo-electrons and secondary electrons. The specifications of our fitting routine are given in Table 1.

After the estimation of c, we compare its value with the minimum of $C(U)$ across all bins. If c is greater than this minimum, which we consider to represent the thermal noise and find at a value of about 3×10^{-3} counts, we subtract c from all counts and perform another fit. This procedure ensures that we do not subtract any counts anymore once the count map has reached the thermal noise level. In any other case, the scheme converges. The final number of background counts are the sum of all extracted c after convergence. At that point, c represents one value of background counts for each 12 min-long window.

After the derivation of c, we correct the number of counts as

$$C_{\text{cor}}(U, \Theta, \Phi, t) = C_{\text{e}^-}(U, \Theta, \Phi, t) + C_{\text{BCK}}(t) - c(t). \tag{9}$$

2.3 Feature aggregation and regression

After extracting the background counts from our EAS data, we correlate the derived EAS background counts c with SEP fluxes, which we denote as 'features' for the purpose of this analysis, in order to establish a quantitative relation between background noise and SEP fluxes. We consider one sample every 12 min by averaging samples in a 12-min window. We linearly combine the SEP flux measurements in the feature vector $\tilde{F}_i$. We apply a normal scaling to the feature vector so that the normally scaled feature vector is

$$F_i = \frac{\tilde{F}_i - \mu_i}{\sigma_i}, \tag{10}$$

where μ_i the mean and σ_i is the standard deviation of the ith feature in the considered set. Each vector of features in a 12-min window is called a 'sample' X_j so that $(X_j)_i = (F_i)_j$. In this notation, i is the index of the feature and j is the time index. We consider only fluxes of energetic electrons, protons, and α-particles in the ranges of energy provided by EPD as our features. The background counts are represented by the dependent variable c_j.

After exposing the correlation between the selected features and the background counts, we reduce the dimensionality of the regression problem with the Ward algorithm for feature agglomeration (Ward 1963). It groups features in clusters, reducing them to their mean for each sample. Groups are formed so that the within-variances are minimized regarding other possible groups, which tends to decrease the correlation of the features with others.

The selection of SEP events in Solar Orbiter data gives us approximately 800 samples to perform our regression. We divide the data points into 70 per cent training data points and 30 per cent evaluation data points, leading to 560 training samples. In a trade-off between generalizability (high number of features to capture the phenomenon) and power of the regression (high number of samples per feature), we choose 25 features for consideration.

We use ordinary least-square (OLS) regression with LASSO regularization to find a linear relation between the features and the dependent variable (Tibshirani 1996). In particular, we minimize

$$\epsilon = \frac{1}{n} \sum_{j=1}^{N_s} \left(c_j - \beta_0 + \sum_{i=1}^{N_f} X_{ji} \beta_i \right)^2 + \lambda ||\boldsymbol{\beta}||_1 \quad (11)$$

with respect to $\boldsymbol{\beta}$, where $\boldsymbol{\beta}$ is the vector of coefficients, the intercept β_0 represents the background counts when there is no energetic particle, N_s is the number of samples, N_f is the number of features, and λ is the regularization factor to be optimized. Due to the LASSO regularization, which is the addition of $\lambda ||\boldsymbol{\beta}||_1$ to the least-square error, there is only one minimum to ϵ.

We minimize the number of non-zero β_i coefficients to capture the SEPs that dominate the creation of background counts and interact most efficiently with the MCP. This regularization minimizes the number of non-zero regression coefficients.

From the regression coefficients, we obtain the physical regression coefficients

$$\beta_{0,\mathrm{phy}} = \beta_0 - \sum_{k=1}^{N_f} \frac{\beta_k}{N_k} \sum_{\ell=1}^{N_k} \frac{\mu_\ell}{\sigma_\ell} \quad (12)$$

and

$$\beta_{i,\mathrm{phy}} = \frac{1}{\sigma_i} \frac{\beta_k}{N_k}, \quad (13)$$

where $\beta_{i,\mathrm{phy}}$ is the physical coefficient of the regression with descaled and individual features, and μ_ℓ and σ_ℓ are the means and the standard deviations of each elementary feature used in the scaling. N_k is the number of features in the kth cluster. In equation (13), the ith feature is in the kth cluster. We evaluate the quality of the regression through the measure

$$C_{\mathrm{BCK,pred}} = \sum_{i=1}^{N_{f,\mathrm{tot}}} \beta_{i,\mathrm{phy}} \tilde{F}_i, \quad (14)$$

where $N_{f,\mathrm{tot}}$ is the total number of features. Based on this result, we introduce the SEP index

$$I_{\mathrm{SEP}} = \frac{1}{\Delta t} C_{\mathrm{BCK,pred}} \quad (15)$$

as a measure for the SEP intensity.

2.4 Simulation of moment computation for PLA

The erroneous counts impact the moment calculation of PLA. For a given index I_{SEP}, we calculate the expected erroneous counts C_{BCK} in PLA measurements as

$$C_{\mathrm{BCK}} = I_{\mathrm{SEP}} \Delta t. \quad (16)$$

We use the PLA performance model to simulate PLA measurements (Nicolaou et al. 2020; Zhang et al. 2024). In a given solar-wind plasma with a given Maxwellian distribution function, we consider the velocity volume scanned by PLA for different look directions and a selected energy range. For each of them, we assume that the number of measured counts without dead time is given by $C_{\mathrm{theo}} + C_{\mathrm{BCK}}$ with uncertainty added through the Poisson error due to finite counting statistics. The number of measured counts C_P then follows a Poisson random process variable of parameter $C_{\mathrm{theo}} + C_{\mathrm{BCK}}$. This distribution is defined as

$$P(C_P) = e^{-(C_{\mathrm{theo}} + C_{\mathrm{BCK}})} \frac{(C_{\mathrm{theo}} + C_{\mathrm{BCK}})^{C_P}}{C_P!}. \quad (17)$$

We assume that the geometric factor is constant and following the PLA specifications with $G = 7.8 \times 10^{-10}$ m^2 sr, the sampling time is set to $\Delta t = 10^{-3}$ s (Nicolaou et al. 2020). We simulate the dead time effect by taking the inverse of equation (3):

$$C_{\mathrm{mes}} = \frac{C_P}{1 + (C_P) \frac{t_d}{\Delta t}}, \quad (18)$$

where C_P is the random variable drawn from the distribution in equation (17). We then obtain the expected measured counts C with dead-time correction to first order by applying equation (3) to C_{mes}.

Integration of the VDF over the full velocity space, based on the previous counts C, defines the moments of the proton VDF. The zeroth moment is the number density:

$$N(t) = \sum_U \sum_\Theta \sum_\Phi \frac{C(U, \Theta, \Phi, t)}{U^2 G \, \Delta t} \Delta U \cos(\Theta) \Delta \Theta \, \Delta \Phi. \quad (19)$$

The components of the bulk velocity are given by the first moment:

$$V_i(t) = \frac{1}{N(t)} \sum_U \sum_\Theta \sum_\Phi U_i \frac{C(U, \Theta, \Phi, t)}{U^2 G \, \Delta t} \Delta U \cos(\Theta) \Delta \Theta \, \Delta \Phi, \quad (20)$$

and the bulk speed is

$$V(t) = \sqrt{\sum_{i=1}^{3} V_i^2(t)}. \quad (21)$$

The temperature tensor elements are given by the second moment of the VDF:

$$T_{ij}(t) = \frac{m}{k_B} \frac{1}{N(t)} \sum_U \sum_\Theta \sum_\Phi (U_i - V_i)(U_j - V_j)$$
$$\times \frac{C(U, \Theta, \Phi, t)}{U^2 G \, \Delta t} \Delta U \cos(\Theta) \Delta \Theta \, \Delta \Phi, \quad (22)$$

and the scalar temperature is

$$T(t) = \frac{1}{3} \sum_{i=1}^{3} T_{ii}(t). \quad (23)$$

3 RESULTS

3.1 Fitting of EAS counts and background extraction

In Fig. 2, we show three different instances of averaged-over-angles counts of electrons as defined in equation (7): one example from a period with almost no detected SEPs (A: 2022 June 30 0:00 UT), one example from an ordinary SEP event (B: 2022 March 21 6:00 UT), and one example from a very strong SEP event (C: 2022 September 6 0:00 UT). We characterize the strength of an SEP event based
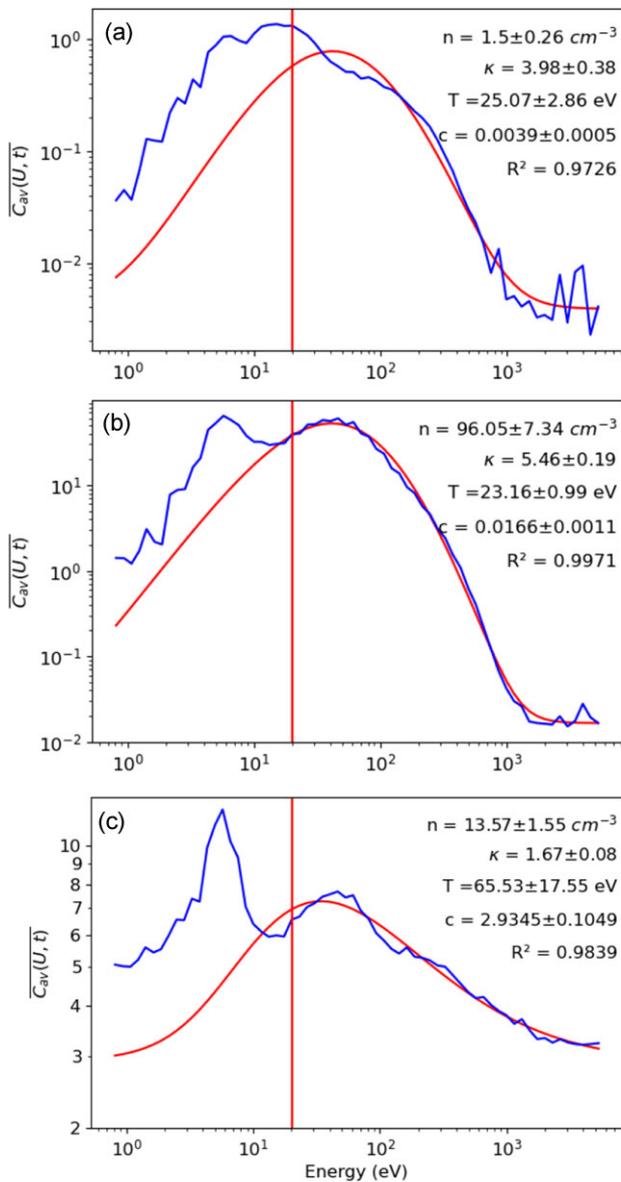
Figure 2. Counts $\overline{C_{av}(U,t)}$ averaged over angles from equation (7) as a function of energy from EAS1 for different SEP situations: (A) no SEP on 2022 June 30 at 0:00 UT; (B) low SEP differential flux on 2022 March 21 at 6:00 UT; (C) high SEP differential flux event on 2022 September 6 at 0:00 UT. The averaging time is 12 min. Smooth curves are fits with modified κ-distribution according to equation (8). Output parameters, coefficient of determination, and 95 per cent uncertainties are displayed in the top-right corners of each plot. The vertical line is the lower bound in energy of our fitting scheme.

on the number of erroneous background counts that we detect. In case A, we detect $3.9\,10^{-3}$ background counts. In case B, we detect $1.7\,10^{-2}$ background counts, and in case C, we detect at the maximum 5.1 background counts. The panels show the number of counts as a function of energy. The blue curve represents the electron data measured by EAS.

We divide the averaged counts in two parts depending on their energy: below 20 eV, photo-electrons are detected – mostly between 3 and 8 eV for (A), and between 3 and 15 eV for (B) and (C). The spectrum for case (C) flattens more at higher energies above 100 eV compared to (A) and (B). It exhibits a high value of averaged counts

at the high-energy end of the tail. While the tails of (A) and (B) are roughly constant, the tail in case (C) still follows a decreasing slope with energy.

We fit the averaged counts measured by EAS in Fig. 2. The fit result is shown in red. In all three cases, the coefficients of determination R are high, matching with a visually appropriate fit result in the energy window in which the fitting is done. Moreover, we observe a greater coefficient R at greater numbers of counts – $R = 0.997$ for (B) with a maximum number of counts of 50, $R = 0.973$ for (A) with a maximum number of counts of 1. As expected, (A) has a low $c = 0.004$, while it is higher in (B) with $c = 0.017$ and very high in (C) with $c = 2.9$. In the first two cases, these values match approximately the minimum of the number of counts at the highest energies. This is not the case in (C) for which the fit function still decreases for the highest energies. The κ-index is likewise lower in (C). The fact that the tail of the fit in case (C) does not reach a plateau indicates that our procedure applies several iterations before reaching the true value of the background counts.

3.2 Correlation between SEP fluxes and background counts

Fig. 3 shows SEP fluxes during event (C), simultaneously with C_{BCK} computed with our fitting. The columns compare C_{BCK} in first row with fluxes of the specified species of SEP in the second and third rows. The second row shows the fluxes measured by HET, and the third row shows the fluxes measured by SIS for protons (left column) and α-particles (middle column), and EPT for electrons (right column). Panel (g) shows low-energy electrons for reference. It has been experimentally verified that electrons in the energy range shown in panel (g) cannot penetrate 2 mm aluminium shielding (Seltzer 1993).

At high SEP fluxes, C_{BCK} is also high, which indicates that the selected SEP fluxes are suitable features for the background count quantification. All shown species have different flux profiles over time, allowing us to isolate their influence on the erroneous counts. Highly energetic protons (panel b) as well as electron fluxes (panel f) rise at around $t = 18\,$h, while the α-particle flux (panel d) grows gradually. At the same time, C_{BCK} increases gradually from 0 to 5 between $t = 15\,$h and $t = 30\,$h. Energetic proton flux (panel b) remains approximately constant for about 30 h, and α-particle (panel d) and electron fluxes (panel f) vary strongly. C_{BCK} decreases between $t = 30\,$h and $t = 35\,$h, approximately at the same time as the energetic electrons (panel f). The least energetic particles fluxes, in panels (c), (e), and (g) rise steeply around $t = 32\,$h, particularly for the α-particles and protons, at the same time as the second increase in C_{BCK}. Panel (f) suggests that the flux in the 1 to 4 MeV is less than the flux at energies greater than 4 MeV. We attribute this inverse spectral scaling as an instrumental artefact. Our regression method is robust against such artefacts as long as the number of reliable features is sufficiently large.

3.3 Regression results

We show the result of our OLS regression with LASSO regularization in Fig. 4. The hyperparameter λ is optimized to obtain the best coefficient of determination. This figure shows $C_{\text{BCK,pred}}$ from equation (14) versus C_{BCK}. The coefficient of determination is high, and high background counts, which are of special interest in the case of PLA, are well captured.

Table 2 gives the coefficients between particle fluxes and erroneous counts in descending order. The most energetic α-particles measured
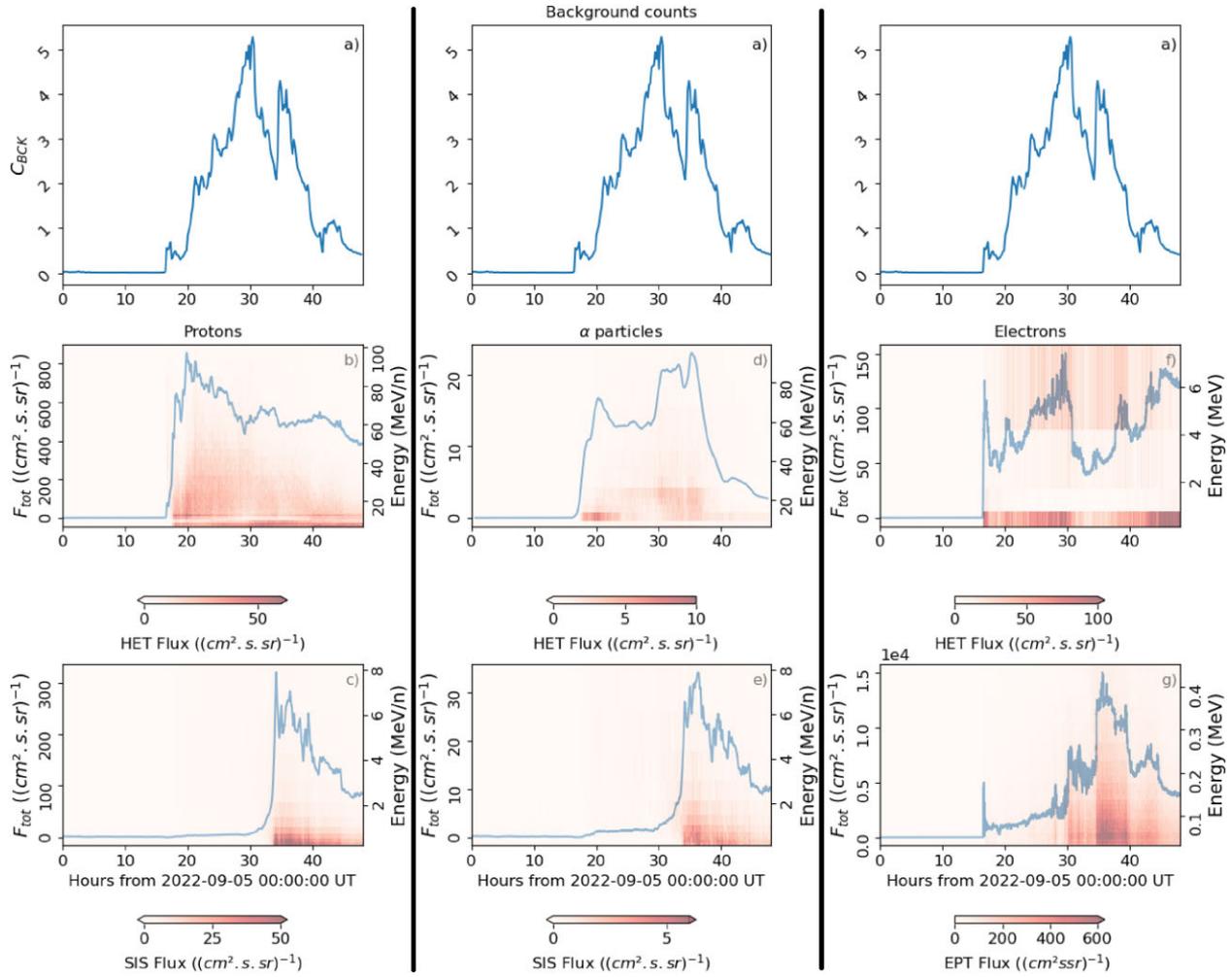
Figure 3. Background counts and SEP fluxes during event (C). Each column is related to a different type of SEP. The first row shows identical plots for C_{BCK} to compare with the different fluxes of the specified SEP species shown in second and third row. In the flux plots, the curve shows the sum of the fluxes F_{tot} for the considered instrument and SEP species from equation (2); the shading indicates the spectral flux. (a) Computed background counts; (b) HET protons flux; (c) SIS protons flux; (d) HET α-particle flux; (e) SIS α-particle flux; (f) HET electron flux; (g) EPT electron flux. The horizontal axis represents time from 2022 September 5 00:00:00 UT.
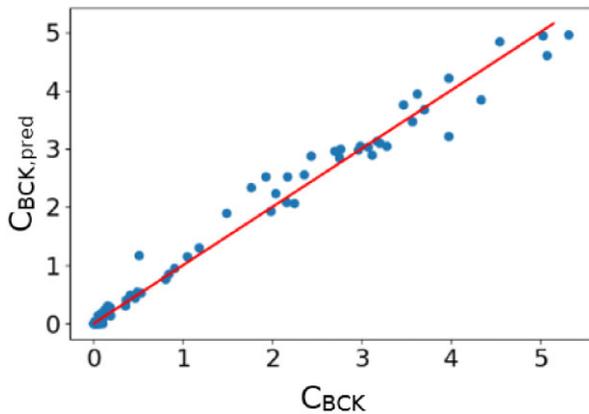
Figure 4. Predicted background counts $C_{BCK,pred}$ versus background counts C_{BCK}, for optimal λ for all test samples. The line shows $C_{BCK,pred} = C_{BCK}$. The coefficient of determination is 0.9876.

Table 2. Elementary feature coefficients and intercept. The description relates to the cluster the feature is agglomerated in. The coefficients are given in $cm^{-2} s^{-1} sr^{-1}$. Only coefficients greater than $1 cm^{-2} s^{-1} sr^{-1}$ are given.

Feature ID ($\tilde{F}_i$)	Description	Coefficient ($\beta_{i,phy}$)
99	HET α (**92–104 MeV n^{-1}**)	26
98	HET α (**76–92 MeV n^{-1}**)	14
35	HET protons (**98–105 MeV**)	5.1
97	HET α (**59–76 MeV n^{-1}**)	3.1
96	HET α (**49–59 MeV n^{-1}**)	2.3
34	HET protons (**89–98 MeV**)	2.2
95	HET α (**41–49 MeV n^{-1}**)	1.1
$\beta_{0,phy}$		−0.0025

are the ones creating the most erroneous counts per interaction with the instrument, with 26 cm^{-2} s^{-1} sr^{-1}.

3.4 Predictions for PLA

We now extrapolate, based on our EAS and EPD results, the impact of SEP events on the accuracy of PLA moment computations. We simulate measurements of PLA under the following representative plasma conditions: $N = 5$ cm^{-3}, $V = 500$ km s^{-1}, $T = 10$ eV, and varying flux F_α of incoming α-particles with energy between 41 and 49 MeV n^{-1}. While α-particles in this energy are not the population creating the most background counts according to Table 2, the number of background counts is only dependent on the SEP index, not on the precise composition of the flux of energetic particles. Therefore, we consider for this extrapolation the chosen F_α as a representative feature of intermediate correlation between SEP flux and erroneous counts. We perform the computation on raw simulated counts and also after the deletion of all measurements with only 1 count to, which is often used in practice (Nicolaou 2023). We averaged the results over 10 executions to cover the variability due to Poisson counting statistics.

Fig. 5 shows the result of this operation, with normalized moments $< Y_{\mathrm{SEP}} > / < Y_{\mathrm{Ref}} >$, where $< Y_{\mathrm{SEP}} >$ is the averaged moment $Y \in (N, V, T)$ computed with background counts added, and $< Y_{\mathrm{Ref}} >$ is the averaged considered reference moment computed without added counts. If $< Y_{\mathrm{SEP}} > / < Y_{\mathrm{Ref}} > \approx 1$, then we consider the impact of SEPs negligible for the calculation of moment Y.

The density computation shows noticeable discrepancy for $F_\alpha \geq 1$ cm^{-2} s^{-1} sr^{-1}. This discrepancy grows significantly, reaching $< N_{\mathrm{SEP}} > / < N_{\mathrm{Ref}} > \approx 30$ for $F_\alpha = 3 \times 10^2$ cm^{-2} s^{-1} sr^{-1}. The 1-count deletion achieves only little improvement. The measured proton bulk speed is less subject to the impact of erroneous counts, with a maximum relative error of about 2 per cent. Temperature is more sensitive to SEP events: for $F_\alpha \geq 10^{-1}$ cm^{-2} s^{-1} sr^{-1}, we find $< T_{\mathrm{SEP}} > / < T_{\mathrm{Ref}} >$ is greater than a factor of 2. A saturation is reached with $< T_{\mathrm{SEP}} > / < T_{\mathrm{Ref}} > \approx 80$ for $F_\alpha \geq 10^2$ cm^{-2} s^{-1} sr^{-1}. The 1-count deletion increases the range of fluxes for which the discrepancy in temperature is less than 2.

4 DISCUSSION

Our fitting routine leads to a reliable representation of the overall shape of the measured counts versus energy. The choice of a modified κ-law to capture the shape of the averaged counts leads, for each of the realized fits, to a coefficient of determination R greater than 0.95. With an increasing number of counts, the relative impact of finite counting statistics decreases, and R increases further. Our knowledge of the VDF allows us to extract information about its tail and, through our iterative procedure, to extract the SEP-generated background counts until the combination of measured counts, background counts, and the fit result are consistent.

We show that the erroneous counts are positively correlated with the fluxes of measured SEPs based on observations from Solar Orbiter's EAS and EPD instruments. The time profile of the fluxes is different for different SEP species, allowing us to separate their contributions to the erroneous counts. Fig. 3 suggests that we must combine the impact of multiple SEP species – protons, electrons, and α particles are the most important species – and multiple SEP energies for a reliable representation of the impact. However, these species and energy ranges contribute with different weights based on the physics of the interaction between the particles and the MCP and the attenuation due to the shielding by the instrument's casing. It
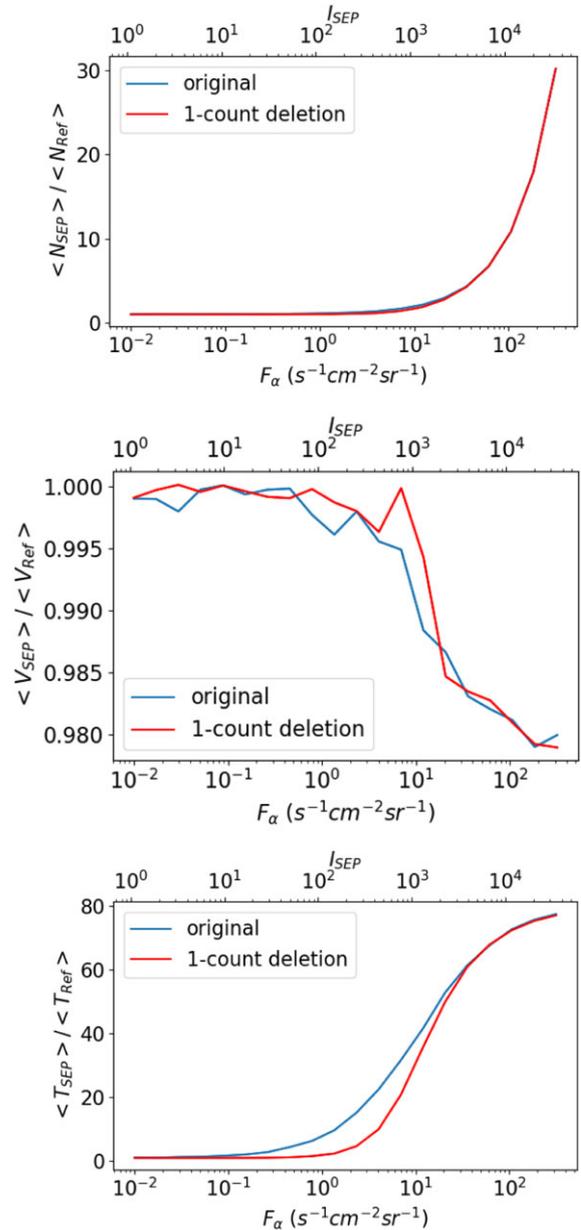
Figure 5. Accuracy of PLA moment computations depending on F_α. Top: Density; Middle: Bulk speed; Bottom: Temperature. The 1-count deletion curve is the result of the computation after setting all the bins with one count to zero. When neglecting all other SEP fluxes, $F_\alpha = 5$ cm^{-2} s^{-1} sr^{-1} corresponds to $I_{\mathrm{SEP}} = 550$ per second, which is the reference value found for event C.

would be interesting to validate our aggregation model for more SEP events beyond the cases shown in this work to create a statistically robust mean impact measure for the effect of SEPs on the detection of thermal particles with instruments like EAS and PLA.

Our regression result has predictive power, with a coefficient of determination greater than 0.98. It is comparable to the model presented by Ramstad et al. (2018) in terms of the prediction accuracy. This previous model uses a genetic optimization algorithm to find the sensitivity coefficients of an electrostatic analyser for energetic particles in the same range as in our study.

The negative value of the intercept $\beta_{0,\mathrm{phy}}$ suggests that we cannot fit a low number of erroneous counts – less than about 0.5 which

corresponds to $I_{SEP} = 50$. According to our results for the physical coefficients $\beta_{i,phy}$, the number of background counts increases with the energy of the incoming SEPs. In most cases, for a given type of SEP, the likelihood of triggering an electron cascade in the MCP increases with the SEP's energy. Moreover, after the first interaction and depending on the geometry of the SEP trajectory through the instrument and spacecraft body, it may have sufficient energy to trigger other electron cascades in different parts of the MCP. The detailed geometrical analysis of this effect is beyond the scope of our work.

Our simulation of PLA measurements during SEP events suggests a non-negligible sensitivity of this instrument to SEPs. Even after a 1-count deletion, the uncorrected directly integrated moments cannot be used during a major SEP event. Since the erroneous counts contribute directly to the density determination as the first moment of the VDF, SEP events lead to a significant overestimation of the proton density with an instrument like PLA. The SEP-triggered erroneous counts lead to a lower proton bulk speed than in the case without SEPs; however, this impact is moderate since the location of the mean speed of the incoming solar-wind protons (first moment) is dominated by the high counts at the centre of the proton beam. Since the temperature is the second moment of the VDF, its determination is strongly affected by the tails of the VDF and thus also by the erroneous counts due to SEPs. These results suggest that the use of on-board integration to determine the solar-wind moments without a reliable correction method would lead to significant misestimations on PLA. On-ground moment calculations, however, would enable the extraction of the background noise due to SEPs with the methods described in this work. Therefore, we recommend not using uncorrected PLA measurements through direct moment integration, even during moderate SEP events, but rather a corrected fitting routine on ground.

As a method to correct for the impact of SEPs, we propose an extraction and deletion of erroneous counts with the same model as shown in Section 2.2. The estimation of the erroneous counts is feasible via a similar fitting routine or by using a controllable variable geometric factor G (for details, see Owen et al. 2020). If the geometric factor is set to a sufficiently low value, the instrument is effectively closed for thermal ions. In this configuration, the counts due to incoming thermal ions are negligible compared to the erroneous counts due to SEPs that enter the instrument from all directions, allowing a nearly direct measurement of the SEP-triggered erroneous contribution. This measurement of the erroneous counts can be used in measurement processing to remove the effect of SEPs. Another solution is the use of a blind sensor anode that is not exposed to any incoming thermal protons. Such a blind anode only measures background counts which can then be subtracted from the measurement signal of the thermal plasma particles. The EPD's Suprathermal Electrons and Protons (STEP) telescope uses this solution (Rodríguez-Pacheco et al. 2020).

5 CONCLUSIONS

This work presents a study of SEP events and their impact on MCPs in Solar Orbiter's EAS. We extrapolate these results to future measurements from Vigil's PLA instrument. Combining fitting, regression, and performance simulations, we show that strong SEP events can significantly deteriorate the accuracy of the computed moments of the solar-wind ions. This effect is particularly strong on the determination of the ion density and temperature. These two quantities are both required for the determination of the ram and thermal pressures of the solar-wind plasma. Since these pressures are key quantities for the determination of the space-weather effects of plasma structures on the magnetosphere, significant inaccuracies in density and temperature would lower Vigil's predictive power for the forecasting of the impacts of high-speed streams and co-rotating interaction regions on Earth. The sensitivity of MCPs to SEPs threatens the accuracy of PLA during extreme SEP events and requires a correction of the detected counts. We propose the use of on-ground moment calculations for PLA combined with a correction method based on a fitting approach that accounts for erroneous counts due to SEPs. Considering that Vigil will serve as an operational space-weather mission, automated and reliable on-ground correction methods would be required in this case in order to keep the measurement latency low and the availability of data high.

As an independent experimental verification of our results, it would be worthwhile to expose a representative PLA unit to energetic particles in a laboratory environment. Even a minimal setup, consisting of MCP, anode board, and shielding, supported by an external power supply, could help understand the fundamental response of the MCP to SEPs better. This work would not replace our modelling efforts since laboratory facilities are not able to expose a device like PLA with plasma conditions representative for the solar wind. In addition, the financial and scheduling impacts of these activities would not be compatible with the Vigil development programme. Nevertheless, we recommend further exploration of possible laboratory radiation tests for the benefit of the development of future plasma detectors.

DATA AVAILABILITY

All data from Solar Orbiter is taken from the Solar Orbiter archive (https://soar.esac.esa.int/soar/). Solar Orbiter is a mission of international cooperation between ESA and NASA, operated by ESA.

REFERENCES

Baker D., 1998, Adv. Space Res., 22, 7
Battersby S., 2019, Proc. Natl Acad. Sci., 116, 23368

Boldyrev S., Forest C., Egedal J., 2020, Proc. Natl Acad. Sci., 117, 9232

Carlson C., Curtis D., Paschmann G., Michel W., 1982, Adv. Space Res., 2, 67

Eastwood J. P. et al., 2024, Space Weather, 22, e2024SW003867

Formisano V., Moreno G., Palmiotto F., Hedgecock P. C., 1973, J. Geophys. Res., 78, 3714

Hands A. D. P., Ryden K. A., Meredith N. P., Glauert S. A., Horne R. B., 2018, Space Weather, 16, 1216

Ladislas Wiza J., 1979, Nucl. Instrum. Methods, 162, 587

Livadiotis G., 2018, Universe, 4, 144

Marov M. Y., Kuznetsov V. D., 2021, in Allahdadi F., Pelton J., eds, Solar Flares and Impact on Earth. Springer International Publishing, Cham, p. 1

Mitchell D. L. et al., 2016, Space Sci. Rev., 200, 495

Müller D. et al., 2020, A&A, 642, A1

Nicolaou G., 2023, Ap&SS, 368, 3

Nicolaou G. et al., 2020, Space Weather, 18, e2020SW002559

Owen C. J. et al., 2020, A&A, 642, A16

Pierrard V., Lazar M., 2010, Sol. Phys., 267, 153

Plan E. L., 2014, CPT Pharmacometrics Syst. Pharmacol., 3, e129

Ramstad R. et al., 2018, Geophys. Res. Lett., 45, 7306

Reames D. V., 2015, Space Sci. Rev., 194, 303

Rodríguez-Pacheco J. et al., 2020, A&A, 642, A7

Seltzer S., 1993, NIST Standard Reference Database, 124

Smith E. J., Davis L., Jones D. E., Colburn D. S., Coleman P. J., Dyal P., Sonett C. P., 1974, Science, 183, 305

Staub J. et al., 2020, J. Space Weather Space Clim., 10, 54

Temmer M., 2021, Living Rev. Sol. Phys., 18, 4

Tibshirani R., 1996, J. R. Stat. Soc. B (Methodological), 58, 267

Ward J. H., 1963, J. Am. Stat. Assoc., 58, 236

Watson G. A., 1978, Numerical Analysis: Proceedings of the Biennial Conference. No. 630 in Lecture notes in mathematics, Springer-Verlag, Berlin

Zhang H., Verscharen D., Nicolaou G., 2024, Space Weather, 22, e2023SW003671

This paper has been typeset from a TeX/LaTeX file prepared by the author.